Advanced Functional Materials

ADVANCED FUNCTIONAL MATERIALS
www.afm-journal.de

RESEARCH ARTICLE OPEN ACCESS

Temperature-Robust Interphase Enables Carboxylate-Ester Electrolyte for Stabilizing High-Voltage Sodium Batteries

Huihua Li[1] | Shuaijie Chang[1] | Hongxu Qu[1] | Jian Wang[2,3] | Fanglin Wu[4] | Minghua Chen[1] | Huang Zhang[1]

[1]School of Electrical and Electronic Engineering, Key Laboratory of Engineering Dielectric and Applications (Ministry of Education), Harbin University of Science and Technology, Harbin, P. R. China | [2]Helmholtz Institute Ulm (HIU), Ulm, Germany | [3]Karlsruhe Institute of Technology (KIT), Karlsruhe, Germany | [4]State Key Laboratory of Advanced Technology for Materials Synthesis and Processing, Wuhan University of Technology, Wuhan, P. R. China

Correspondence: Huihua Li (li.huihua@hrbust.edu.cn) | Jian Wang (jian.wang@kit.edu; wangjian2014@sinano.ac.cn) | Minghua Chen (mhchen@hrbust.edu.cn) | Huang Zhang (zhang.huang@hrbust.edu.cn)

Received: 1 December 2025 | **Revised:** 3 February 2026 | **Accepted:** 5 February 2026

Keywords: electrolyte additive engineering | high-voltage cathode | interphase stability | sodium metal batteries | wide temperature application

ABSTRACT

High-voltage sodium metal batteries (SMBs) under wide temperature are fundamentally contingent upon the electrochemical stability of electrode-electrolyte interfaces. Although carboxylate esters offer a pathway to superior low-temperature performance, their inherent low oxidative stability presents a major impediment. Herein, a synergistic electrolyte engineering strategy of employing ethyl acetate (EA) with vinylene carbonate (VC) as multifunctional additives is initially pioneered. Despite its weak coordination with Na^+, the introduced VC serves as an effective regulator that restructures the solvation shell and preferentially decomposes in synergy with PF_6^- anions, thereby constructing a robust cathode electrolyte interphase (CEI). As confirmed by X-ray spectroscopies and electronic microscopes, this ultrathin but gradient architecture comprises a flexible but fluorine-rich organic outer layer and a mechanically robust with ionically conductive inner layer enriched with NaF/Na_3PO_4, extending the stability of high-voltage O3-type $NaNi_{1/3}Fe_{1/3}Mn_{1/3}O_2$ (NFM) cathode and suppressing transition metal dissolution. Consequently, the NFM||Na cells achieve exceptional performance, demonstrating a capacity retention of 74.6% after 200 cycles under 4.5 V. Even decreasing the surrounding temperature to −20°C, a high capacity retention of 91.3% is achieved, and the NFM||hard carbon full cells maintain the Coulombic efficiency as high as 99.3% over 100 cycles, enabling high-voltage operation and wide-temperature tolerance for high-energy-density SMBs.

1 | Introduction

Recently, high-voltage sodium metal batteries (SMBs) have emerged as one of the most promising battery technologies owing to the abundant sodium resources and their potential to deliver high energy densities [1–3]. Yet their commercial viability is undermined by two entwined failure modes. At the anode, the extreme reactivity of sodium drives spontaneous electrolyte decomposition, resulting in the formation of a fragile solid-electrolyte interphase (SEI) that fails to regulate uniform metal plating. Consequently, sodium metal tends to grow in mossy or dendritic morphologies, accompanied by the accumulation of electrically isolated "dead" sodium, which increases the risk of internal short circuits and thermal runaway [4–6]. In parallel, high-voltage cathodes suffer from oxidative degradation of the electrolyte, continuous reconstruction of the cathode-electrolyte interphase (CEI) [7, 8], and intergranular crystalline cracking, all of which accelerate capacity decay and gas generation [9–11]. Therefore, the simultaneous stabilization of both anode and cathode interfaces represents a critical challenge and a prerequisite for the development of safe, high-energy SMBs.

To address these aforementioned tough issues, a variety of strategies have been proposed, which include the development of advanced 3D Na hosts [12, 13], an artificial SEI protective layer [14–16], and electrolyte engineering [17–19]. Among the available strategies, electrolyte engineering stands out for its operational simplicity and interfacial efficacy. While many approaches require complex electrode pre-treatment or incorporation of auxiliary materials, this method simply introduces functional additives directly into the electrolyte, facilitating the in situ formation of protective interphases on both cathode and anode during electrochemical cycling. Crucially, a rationally designed electrolyte can simultaneously stabilize high-voltage cathodes by forming a robust CEI while protecting the anode via a durable SEI. This additive-driven interfacial engineering approach has proven highly effective in enhancing cycling stability for high-capacity electrodes [20, 21]. Indeed, electrolyte engineering has emerged as a powerful and versatile strategy for interfacial stabilization across various metal battery systems, including Li and Zn batteries [22–24]. As reported, linear carboxylic acid esters demonstrate resistance to decomposition at elevated temperatures and avoidance of solidification at low temperatures, positioning them as ideal solvent candidates for wide-temperature-range electrolytes [25, 26]. For example, lithium bis(fluorosulfonyl)imide (LiFSI) electrolyte in methyl propionate/fluoroethylene carbonate (9:1 v/v) was investigated for wide-temperature Li batteries [27]. Moreover, by introducing weakly-coordinated methyl butyrate as cosolvent to tune ion-dipole and dipole-dipole interactions, an anion-reinforced, fluorine-free carboxylate ester electrolyte builds inorganic-rich interphases that enable Prussian blue||hard-carbon cells to cycle stably from −20 to 100°C, retaining 91% capacity after 230 cycles at 55°C [28].

Alternatively, as a typical linear carboxylic acid ester, ethyl acetate (EA) demonstrates considerable promise for wide-temperature-range electrolytes application due to its low freezing point (−83.6°C), high boiling point (77.2°C), low viscosity, and cost-effectiveness [29, 30]. However, linear carboxylic esters also face critical challenges as electrolyte solvents in batteries, including low intrinsic conductivity of pure solvents, difficulty in tuning the solvation shell, narrow voltage window, and chemical corrosion toward cathode degradation [30, 31]. Several strategies have been adopted to improve the compatibility of EA-based electrolytes in batteries [30]. The incorporation of 5 wt.% FEC into 1 ᴍ $NaPF_6$-EA electrolytes orchestrates the formation of a robust, NaF-rich organic-inorganic composite SEI and CEI on both electrodes, enabling the $Na_{0.97}Ca_{0.03}[Mn_{0.39}Fe_{0.31}Ni_{0.22}Zn_{0.08}]O_2$/hard carbon (HC) pouch cells cycled up to 4.0 V at 40°C a lengthy cycling lifetime of 250 cycles with ~80 % capacity retention [32]. That means the intrinsically poor interfacial compatibility between carboxylate esters and the carbonaceous anode can be effectively mitigated by adopting either high-concentration electrolytes or fluorinated co-solvent engineering. Nevertheless, EA is still stifled by a narrow electrochemical window (<4.2 V vs Na^+/Na) and interfacial chemistry that is simultaneously corrosive to Na metal and catastrophically oxidized at high-voltage cathodes, leaving it barely viable for practical high-energy SIBs [33–36]. Therefore, electrolyte optimization must evolve beyond simple solvent selection, demanding precise molecular engineering to widen the redox limits and construct resilient, multifunctional interphases.

In this work, for the first time, we have adopted vinylene carbonate (VC) as a multifunctional additive to enable EA-based electrolytes to operate stably at a high cut-off voltage of 4.5 V, breaking through the application bottleneck of carboxylate ester electrolytes in high-voltage sodium batteries. As optimized, a formulated electrolyte of 2.0 ᴍ $NaPF_6$ in EA with 5 vol% VC (EA+5VC) simultaneously suppresses solvent oxidation and reconfigures the interfacial chemistry. Consequently, the electrolyte exhibits significantly enhanced stability against a 4.5 V-class $NaNi_{1/3}Fe_{1/3}Mn_{1/3}O_2$ (NFM) cathode, attributable to the formation of a robust and highly electronically insulating cathode electrolyte interphase (CEI) as comprehensively investigated by X-ray spectroscopies and electronic microscopes. The NFM-Na cells employed with optimized electrolyte under 4.5 V display exceptional cycling stability, demonstrating a capacity retention of 74.6% at 0.1 A g^{-1}. Furthermore, when paired with a hard carbon (HC) anode in a full cell (NFM||HC), the system delivers a remarkable cycling performance with an initial discharge capacity of 96.8 mAh g^{-1} and an average Coulombic efficiency of 99.3% over 100 cycles at 0.1 A g^{-1} within a 2.0–4.3 V, showing the potentials in high-voltage sodium battery systems.

2 | Results and Discussion

As schematically illustrated in Figure 1a, the VC functions as an effective film-forming additive that stabilizes the electrode interface via its active participation in the solvation structure. The highest occupied molecular orbital (HOMO) and lowest unoccupied molecular orbital (LUMO) energies provide quantitative descriptors for screening intrinsic oxidation and reduction limits, respectively, thereby establishing a reliable hierarchy of redox stability among electrolyte constituents. As exhibited in Figure 1b, the vinylene carbonate (VC) possesses the highest HOMO energy among all constituents, predisposing it to preferential oxidative decomposition at the cathode surface. Concomitantly, its LUMO (−0.51 eV) is lower than that of ethyl acetate (0.01 eV), ensuring kinetically favorable reductive breakdown on metallic sodium [37–39]. This dual redox susceptibility renders VC an effective sacrificial additive for the synchronous formation of robust SEI and CEI layers on both electrodes. In addition, the solvating capability of EA and VC solvents was examined by calculating the binding energies of Na^+ with EA and VC molecules using Density Functional Theory (DFT), as shown in Figure 1c. The binding energy of EA with Na^+ (−21.45 kcal mol^{-1}) is slightly higher than that of VC (−19.30 kcal mol^{-1}), indicating a relatively strong participation of EA in the solvation structure.

Figure 1d presents the solvation structure obtained from molecular dynamics (MD) simulations to provide a more comprehensive understanding of the electrolyte. For the interaction between Na^+ and F in PF_6^-, the first peak appears at approximately 0.24 nm, with an average coordination number of about 2.78. This indicates that PF_6^- anions are actively involved in forming the primary solvation shell. In contrast, the interaction pair between Na^+ and O in VC also shows a first peak near 0.24 nm, but with an extremely low coordination number (0.18). This quantitatively confirms that VC molecules rarely enter the primary solvation shell of Na^+. While the interaction between Na^+ and O in EA exhibits the strongest coordination characteristics, with the

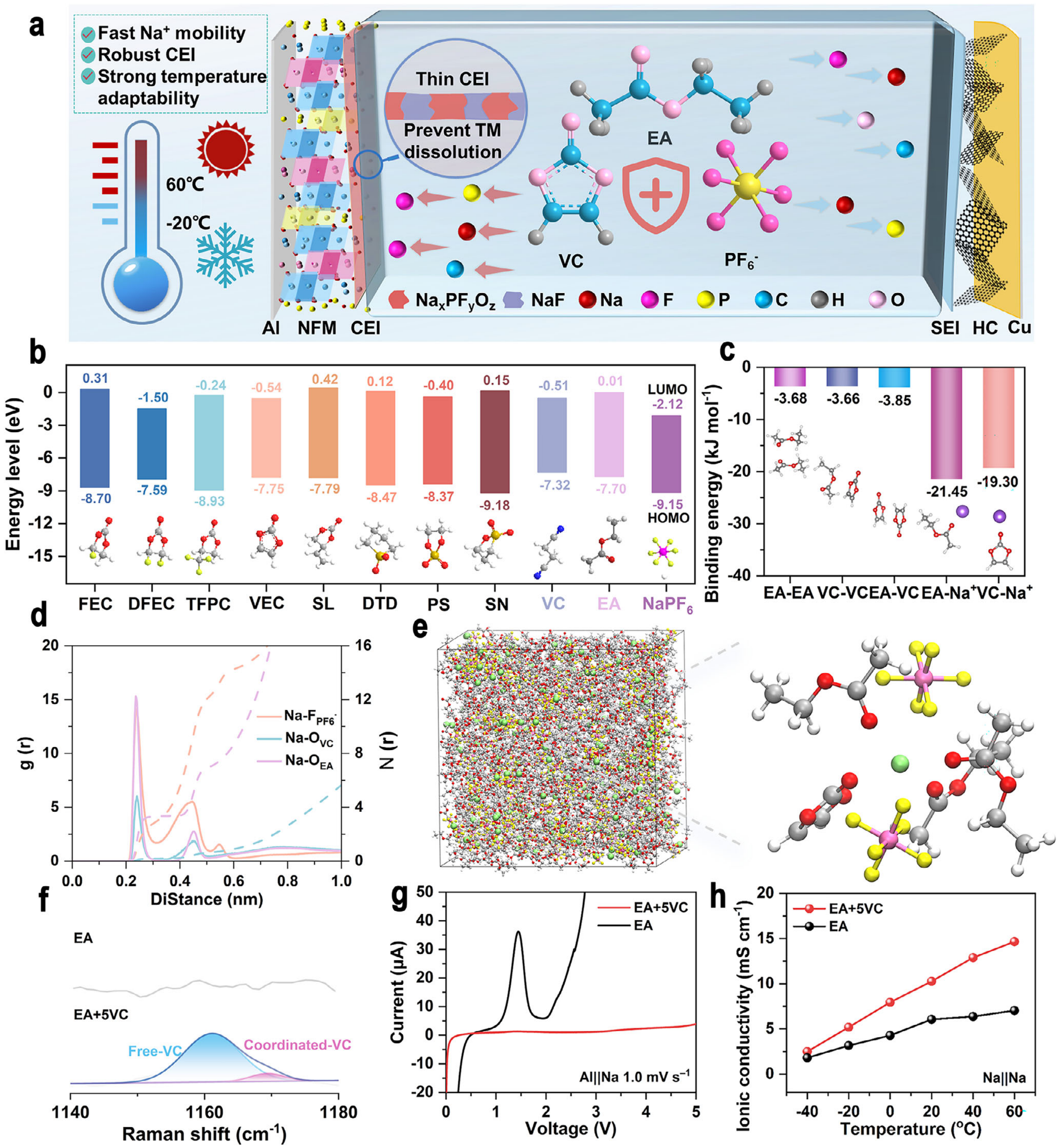

FIGURE 1 | (a) Schematic representation of the electrolytic structure. (b) Theoretical calculation of LUMO and HOMO values of different additives. (c) The binding energy of sodium ions with EA and VC. (d) Radial distribution functions (solid lines) and coordination numbers (dotted lines) calculated from MD simulations in EA+5VC. (e) Snapshots of the solvation structure of EA+5VC. (f) Raman spectra of the characteristic peaks of VC in electrolytes. (g) LSV curves of EA and EA+5VC from 0.0 to 5.0 V with a scan rate of 1.0 mV s^{-1}. (h) Ionic conductivity of EA and EA+5VC electrolyte over a temperature range from −40 to 60°C.

first peak located at 0.236 nm and a high coordination number of 3.31, clearly establishing EA as the dominant coordinating solvent for Na$^+$. A comprehensive analysis of the solvation structure of EA+5VC electrolyte was illustrated, with representative snapshots of the solvation sheath depicted in Figure 1e. Na$^+$ is primarily surrounded by EA molecules and PF_6^- anions, forming a tightly primary solvation shell. In contrast, VC molecules are mostly distributed outside the solvation shell, indicating that VC does not significantly alter the original solvation structure.

Practically, Raman spectroscopy was performed to identify the solvation structure (Figure S1). The pristine EA exhibits distinct peaks at 844.7 and 632.7 cm^{-1}, corresponding to C—C stretching and C—O bending vibrations, respectively, while VC shows the characteristic band at approximately 904.9 cm^{-1}, assigned to C—O stretching mode. In the EA-based electrolyte comprising 2.0 M NaPF$_6$, the P—F stretching mode of the PF$_6$$^-$ anion was observed, while the C—O bending vibration of EA shifted slightly to a higher wavenumber relative to that of the EA solvent due to coordination with Na$^+$ [40, 41]. Notably, the characteristic stretching band of coordinated EA at 632.7 cm^{-1} exhibits no discernible shift when VC is added, from 1% to 20% (Named as EA+*x*VC), indicating that the presence of VC does not markedly alter the solvation interaction between EA and Na$^+$. The Raman spectra were further analyzed to identify the coordination states of EA and PF$_6$$^-$ anion, as shown in Figure S2. A prominent band observed at 844.7 cm^{-1} is attributed to the vibration of free EA molecules, while the peak at 850.5 cm^{-1} corresponds to EA coordinated to Na$^+$. It is worth noting that, compared to the pure EA electrolyte, the proportion of coordinated EA in the EA+5VC electrolyte does not change significantly. This observation is consistent with the results of the vibrational peaks of EA. As shown in Figure 1f, deconvolution analysis of VC further confirms that the proportion of free VC molecules is dominant, while the solvated VC one is negligible. That means its molecules scarcely enter the solvation sheath of Na$^+$—a conclusion supported by the extremely low proportion of VC molecules in the coordinated state. Additionally, the PF$_6$$^-$ anion is actively involved in solvation structure, facilitating the formation of anion-derived interphases. Fourier transform infrared spectroscopy (FT-IR) was further employed to elucidate the solvation structures (Figure S3). The distinct Raman bands observed at 1161.1 cm^{-1} (free VC) and 1169.4 cm^{-1} (coordinated VC) demonstrate that VC participates in the solvation structure in only a negligible proportion, and most VC molecules remain uncoordinated in the bulk electrolyte instead of entering the primary solvation sheath of Na$^+$. Consistent with Raman observations, the EA+5VC electrolyte exhibits a reduced proportion of coordinated EA and VC (Figure S4). The collective spectroscopic evidence confirms that VC primarily functions as a dilute, which can improve the ionic conductivity.

Linear sweep voltammetry (LSV) was performed to evaluate the electrochemical stability of the electrolytes (Figure 1g). The EA electrolytes exhibit a distinct reduction peak at around 1.5 V, which is attributed to the irreversible reduction and decomposition of EA solvent molecules on the highly reactive bare sodium metal surface. Notably, the introduction of 5 vol% VC completely suppresses this peak, directly demonstrating that VC can be preferentially reduced at a higher potential to form a protective SEI film. This effectively shields the sodium anode and blocks the detrimental decomposition pathways of the EA solvent. The EA+5VC electrolyte exhibits an extended oxidation stability beyond 5 V. As shown in Figure S5, the electrolyte containing 5 vol% VC exhibits superior oxidative stability and interfacial compatibility with Na metal during linear sweep voltammetry (LSV) measurement. Wetting behavior tests on commercial aluminum foil (Figure S6) reveal that the EA+5VC electrolyte achieves the smallest contact angle (28.4°), superior to those of the EA (39.8°) and conventional EC/DEC (37.9°) electrolytes, suggesting facilitated ion-sorption dynamics [42, 43]. Ionic conductivity measurements across a wide temperature range (-40°C to 60°C) reveal that the EA+5VC electrolyte exhibits markedly higher conductivity than both the blank EA electrolyte and other VC-containing formulations (Figure 1h; Figure S7). This enhancement stems from VC-induced reorganization of the electrolyte's microstructure [44]. As demonstrated by spectroscopic results, VC significantly reduces the proportion of EA molecules in Na$^+$ primary solvation sheath while increasing free PF$_6$$^-$ abundance. Since VC exhibits weaker Na$^+$ binding energy than EA, it functions as a dilute that disrupts the dense EA-dominated coordination network, creating a locally concentrated electrolyte environment with enhanced molecular disorder [45, 46]. This structural rearrangement reduces solution viscosity and facilitates ion migration, enabling maintained fluidity and conductivity even at −40°C. In contrast, the conventional EC/DEC electrolyte shows inferior conductivity from −20°C to 60°C and suffers dramatic performance degradation below−20°C, confirming its limitation for wide-temperature applications.

To validate the practical performance of the designed optimal electrolyte, sodium metal batteries were assembled and employed with an O3-type NaNi$_{1/3}$Fe$_{1/3}$Mn$_{1/3}$O$_2$ (NFM) cathode. The EA electrolyte (2 M Na PF$_6$ in EA) possesses an oxidation limit below 2 V vs Na/Na$^+$, precluding its capability with the NFM cathode. This result highlights the fundamental limitations of the unmodified EA-based electrolyte for high-voltage sodium batteries. For better comparison, the commercial 1 M NaPF$_6$ EC/DEC formulation (denoted EC/DEC) was also employed as the control one. Cyclic voltammetry (CV) profiles (Figure 2a) were compared between 2 and 4.3 V at a scan rate of 0.1 mV s^{-1}. The results reveal that the NFM||Na cell with EA+5VC electrolyte exhibits larger integrated peak areas and almost perfectly overlapping sweeps, whereas the EC/DEC-based cell delivers smaller and progressively distorted peaks. The cycling stability performance at a low current density of 0.1 A g^{-1} was evaluated in the range of 2–4.3 V (Figure 2b). The cell with EC/DEC electrolyte exhibits poor cycling performance, retaining only the capacity retention of 54.4% after 200 cycles with an average Coulombic efficiency (CE) of 96.2%. In contrast, the cell with optimized EA+5VC electrolyte demonstrates higher specific capacity with a higher capacity retention of 76.7% and a superior average CE of 99.4%, indicating the excellent compatibility of the optimal electrolyte with NFM-based SMBs. Moreover, the electrolyte containing VC also increases the initial CE from 80.0% (EC/DEC) to 95.0% and boosts the first-cycle discharge capacity from 104 to 144 mAh g^{-1} (Figure S8), indicating the improved reversibility of Na$^+$ (de)intercalation reactions. For a more comprehensive evaluation, the cycling performance of NFM||Na cells employing the same concentration (2 M NaPF$_6$) in EC/DEC electrolyte was also examined under identical conditions (Figure S9). Although the cell with EC/DEC(2 M) delivered a slightly higher initial discharge capacity, it suffered from a more rapid capacity fade, retaining only 46.4% of its capacity after 200 cycles, which is far behind the optimal electrolyte as well.

As shown in Figure S10, a systematic comparison between 1 M and 2 M EA+5VC electrolytes paired with the NFM cathode clearly demonstrates the superiority of the higher concentration. The 2 M system provides an initial discharge specific capacity of 141.95 mAh g^{-1}, higher than that of 124.73 mAh g^{-1}. More importantly, the cell with 2 M electrolyte exhibits markedly enhanced cycling stability, maintaining substantially higher capacity retention after 100 cycles. This performance advantage establishes 2 M NaPF$_6$ as the optimal base concentration for our study. Furthermore, evaluation of various VC-containing electrolytes reveals that the EA+5VC formulation achieves the most stable

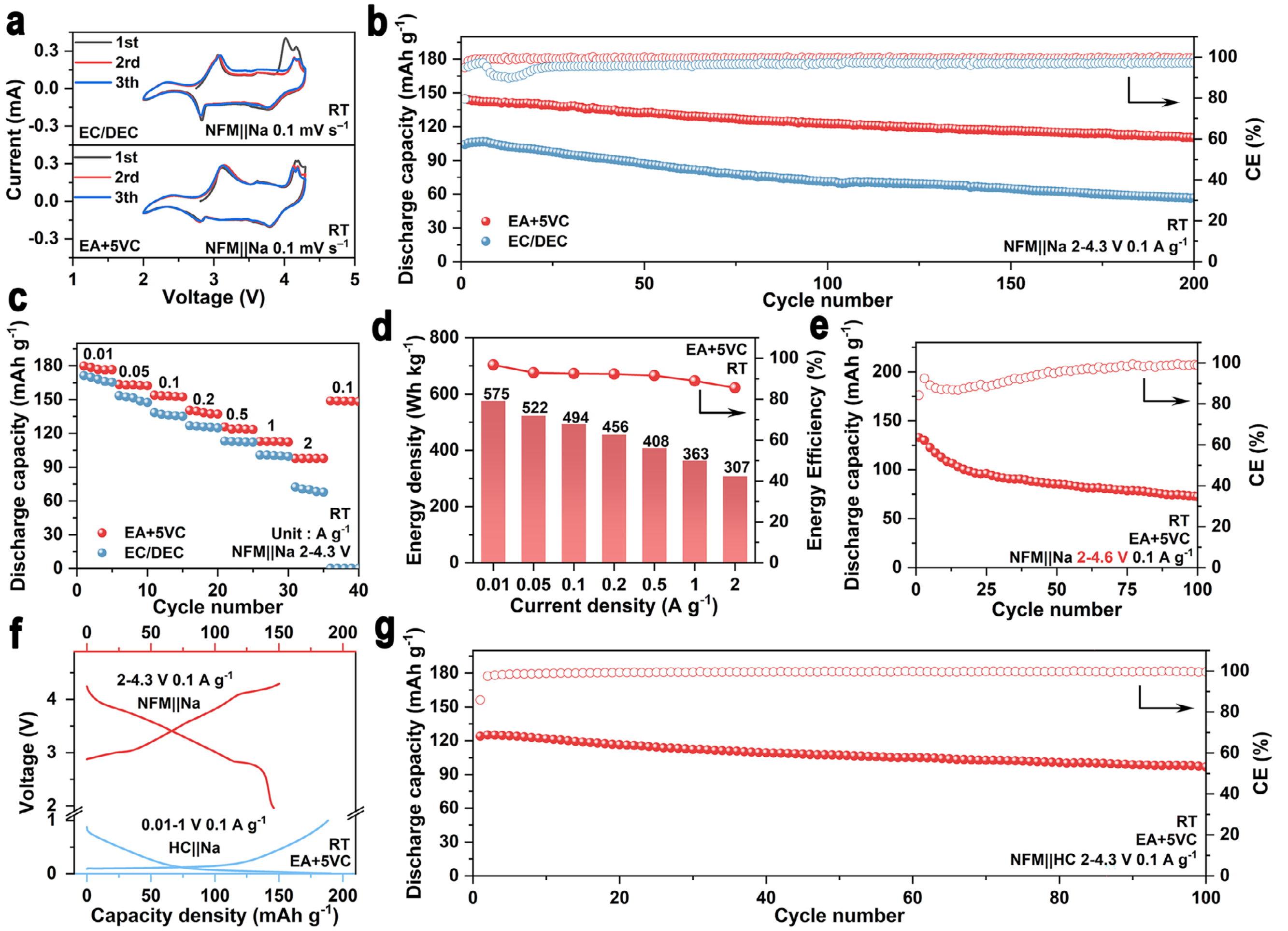

FIGURE 2 | (a) CV curves of NFM||Na cells using EC/DEC and EA+5VC electrolytes in the voltage range of 2–4.3 V with a scan rate of 0.1 mV s^{-1}. (b) Cycling performance of NFM||Na cells using EC/DEC and EA+5VC in the voltage range of 2–4.3 V at 0.1 A g^{-1}. (c) Rate performance of NFM||Na cells using EC/DEC and EA+5VC with the multiple discharge rates at 0.01, 0.05, 0.1, 0.2, 0.5, 1, and 2 A g^{-1}. (d) Energy efficiency and energy density of NFM||Na cells with EA+5VC. (e) Cycling performance of NFM||Na cells using EA+5VC in the voltage range of 2–4.6 V at 0.1 A g^{-1}. (f) Galvanostatic charge-discharge curves of the NFM cathode and the HC anode. (g) Cycling performance of NFM||HC cells using EA+5VC in the voltage range of 2–4.3 V at 0.1 A g^{-1}.

cycling performance with minimal voltage hysteresis. Based on its superior ionic conductivity, widened electrochemical window, and exceptional cycling stability, 5 vol% VC was identified as the optimal additive concentration, providing the foundation for our high-performance electrolyte system. The rate performance in Figure S11 also confirms the better power capability of the EA+5VC electrolyte. Based on the highest ionic conductivity, enhanced electrochemical window, and the most stable cycling performance, 5 vol% VC was identified as the optimal choice. Figure 2c shows that the NFM||Na cell employing EA+5VC electrolyte also displays superior rate performance, achieving much higher discharge capacities of 179.8, 163.4, 154.0, 140.6, 125.7, 112.8, and 97.8 mAh g^{-1} at 0.01, 0.05, 0.1, 0.2, 0.5, 1.0 and 2.0 A g^{-1}, respectively, compared with the cell using commercial EC/DEC electrolyte. Energy density analysis based on the mass of NFM (Figure 2d; Figure S12) further revealed that the EA+5VC system achieves 575 Wh kg^{-1} with an average output voltage of 3.23 V at 0.01 A g^{-1}. Even at a higher current density (2 A g^{-1}), the cell can still maintain an energy density of 307 Wh kg^{-1} and an energy efficiency of 85.59%, which is significantly higher than the EC/DEC system of 147 Wh kg^{-1} and 73.35% under the same conditions, demonstrating its superior power and energy densities of EA+5VC electrolyte capable of practical applications. Furthermore, when the upper-cut-off voltage is raised to 4.5 V, the NFM||Na cell with EA+5VC still delivers an initial discharge capacity of 149 mAh g^{-1} with 74.6% retention after 200 cycles at 0.1A g^{-1} (Figures S13 and S14), demonstrating robust compatibility even under aggressive high-voltage conditions.

To highlight the compatibility of the electrolyte at high voltage ranges, the NFM||Na battery was evaluated under the cut-off voltage of 4.6 V. As shown in Figure 2e, the battery with EA+5VC electrolyte stably operated for over 100 cycles, where the extended working voltage (4.6 V) exceeds the upper limit of the typical ester-based electrolytes (≤ 4.4 V). Moreover, the compatibility of the EA+5VC electrolyte with the high-voltage cathode material $Na_3V_2(PO_4)_2F_3$ (NVPF) was also confirmed across different cut-off voltage ranges (4.0–4.5 V) (Figure S15). The above results indicate that the EA+5VC electrolyte effectively extends the stable working window of carboxylate ester-based electrolytes to higher voltage regions (≥4.5 V). To broaden the compatibility of the EA+5VC electrolyte with different electrodes,

$Na_4Fe_3(PO_4)_2(P_2O_7)$ (NFPP)||Na cells were assembled and tested in the range of 2.5–4 V (Figure S16). At 0.5 A g^{-1}, the NFPP||Na cell with EA+5VC electrolyte delivers a discharge specific capacity of 88 mAh g^{-1} and maintains 95.7% of the initial capacity after 700 cycles, demonstrating remarkable cyclic stability within polyanion cathodes. Moreover, the HC||Na cell was also assembled for further evaluation. Moreover, when the mass loading is increased to 12.53 mg cm^{-2}, the NFM||Na cell can still operate stably (as shown in Figure S17), which confirms that the optimized electrolyte can support stable cell operation even under the demanding conditions of thick electrodes.

As shown in Figure S18, the HC||Na cell with EA+5VC electrolyte delivers a discharge specific capacity of 170 mAh g^{-1} with an average CE of 99.4% at 0.1 A g^{-1}. Inspired by the superior compatibility of EA+5VC electrolyte with both cathode and anode, NFM||HC full cells were fabricated with a balanced capacity ratio of 1.2 (anode/cathode) based on the individual electrode voltage profiles in EA+5VC (Figure 2f). As shown in Figure 2g, the NFM||HC full cell in the range of 2–4.3 V achieves an initial discharge capacity of 96.8 mAh g^{-1} and a capacity retention of 77.7% after 100 cycles under 0.1 A g^{-1} with an average CE of 99.3%. The charge/discharge profiles of the initial five cycles almost perfectly overlap, indicating negligible polarization and excellent kinetics (Figure S19). To situate the performance of our VC-modified EA electrolyte within the current landscape, a systematic comparison was conducted against high-performance electrolyte systems reported in recent literature for high-voltage SMBs (Table S1). These results confirm that the EA+5VC electrolyte simultaneously stabilizes the high-voltage NFM cathode and the HC anode, enabling a durable, high-energy sodium-ion full-cell for practical applications.

Ex-situ XRD analysis was conducted on NFM electrodes after 20 cycles at 0.1 A g^{-1} (2.0–4.3 V) in EA+5VC and EC/DEC electrolytes. This specific cycle number was selected as it represents a critical juncture where the performance disparity between the two electrolytes becomes fully evident. As indicated in Figure 2b, the EC/DEC system exhibits pronounced Coulombic efficiency fluctuation and capacity decay by this stage, indicating substantial interfacial instability. In contrast, the EA+5VC system maintains exceptional electrochemical stability. This comparison at the 20-cycle mark enables direct correlation between electrolyte composition and NFM structural integrity, providing compelling evidence for the protective capability of our designed electrolyte under high-voltage operation. In Figure 3a,b, the NFM electrode cycled in the EA+5VC electrolyte maintains well-defined diffraction peaks corresponding to the (003), (006), (101), (012), and (104) planes, with negligible peak shifts compared to the pristine material, indicating excellent preservation of the layered structure. In sharp contrast, the electrode cycled in EC/DEC electrolyte suffers from substantial structural degradation, characterized by significant attenuation of the (003) and (006) peaks and near-complete disappearance of the (101), (012), and (104) reflections. This marked difference originates from the superior interfacial protection afforded by the VC-modified EA electrolyte, which forms a stable CEI that effectively suppresses electrolyte oxidation and subsequent acidic attack on the cathode lattice. Consequently, the structural integrity of NFM is preserved in EA+5VC, whereas conventional EC/DEC electrolyte undergoes oxidative decomposition at high voltage, generating aggressive species that trigger cathodic degradation and ultimately lead to structural collapse [47]. Indeed, by using inductively coupled plasma mass spectrometry (ICP-MS) measurement, the dissolution behavior of transition metals (Ni, Fe, Mn) in the NFM cathode material after cycling was quantified, as shown in Figure 3c. The ICP-MS quantification (Table S2) clearly reveals severe transition metal dissolution from the NFM cathode in EC/DEC electrolyte, with Fe ion concentration reaching 24.57 g kg^{-1} after 20 cycles at 4.3 V, directly indicating the inadequate interfacial protection provided by this conventional electrolyte system. Specifically, the severe Fe dissolution is attributed to the lower octahedral-site-preference energy (OSPE) of Fe^{3+} relative to Ni^{2+} and Mn^{3+}, which weakens its bonding within the transition-metal slab and promotes migration into the electrolyte. The excessive Fe dissolution triggers cathode structural degradation and an O3-to-P3 phase transition in EC/DEC electrolyte, thereby accelerating capacity fading [48]. In contrast, metal concentrations in separators from EA+5VC cells fall below the detection limit, evidencing that the VC-derived interphase effectively immobilizes transition metals and maintains structural integrity.

To visually identify the structural degradation, scanning electron microscopy (SEM) was performed on the cycled NFM electrodes after 20 cycles. As shown in Figure S20, the NFM electrodes cycled in VC-containing electrolytes show no significant cracking. The amplified SEM images (Figure 3d,e) reveal well-maintained particle integrity after cycling in EC/DEC and EA+5VC electrolytes, respectively. After 20 cycles at 4.3 V, secondary-electron images reveal a micro-cracked, highly fractured surface on NFM particles extracted from EC/DEC cells. Conversely, NFM particles cycled in EA+5VC exhibit an intact, smooth morphology, underscoring that the VC-derived interphase effectively shields the cathode from mechanical degradation and preserves both particle and structural integrity. High-resolution transmission electron microscopy (HRTEM) characterization was used to distinguish the crystallographic divergence of the NFM electrode after cycling in different electrolytes. As shown in Figure 3f,g NFM cycled in EC/DEC electrolyte shows disrupted lattice fringes, featured by diffuse diffraction contrast, discontinuous fringes, and localized distortions that signal an O3 → P3 phase transformation. Notably, the measured interplanar spacing of the (104) lattice fringe expands to approximately 0.219 nm in the EC/DEC-cycled sample, representing a detectable expansion from the characteristic spacing of pristine O3-phase NFM (0.216 nm). This lattice distortion provides direct evidence for the detrimental phase transition occurring under high voltage. In contrast, the cathode cycled in EA+5VC maintains the original (104) spacing of 0.216 nm with well-defined lattice fringes, demonstrating exceptional structural coherence and confirming effective suppression of phase transformation. These observations substantiate that the VC-derived interphase successfully preserves the O3-type layered structure under aggressive cycling conditions [49].

In addition, electrochemical impedance spectroscopy (EIS) highlights distinct interfacial evolution in NFM||Na cells using different electrolytes. After 20 cycles at 4.3 V, the cell with EC/DEC electrolyte exhibits a significant increase in interfacial resistance (Figure S21a). However, the cell employing EA+5VC demonstrates a neglectable evolution in interfacial resistance (Figure S21b), indicative of a self-limiting and highly stable

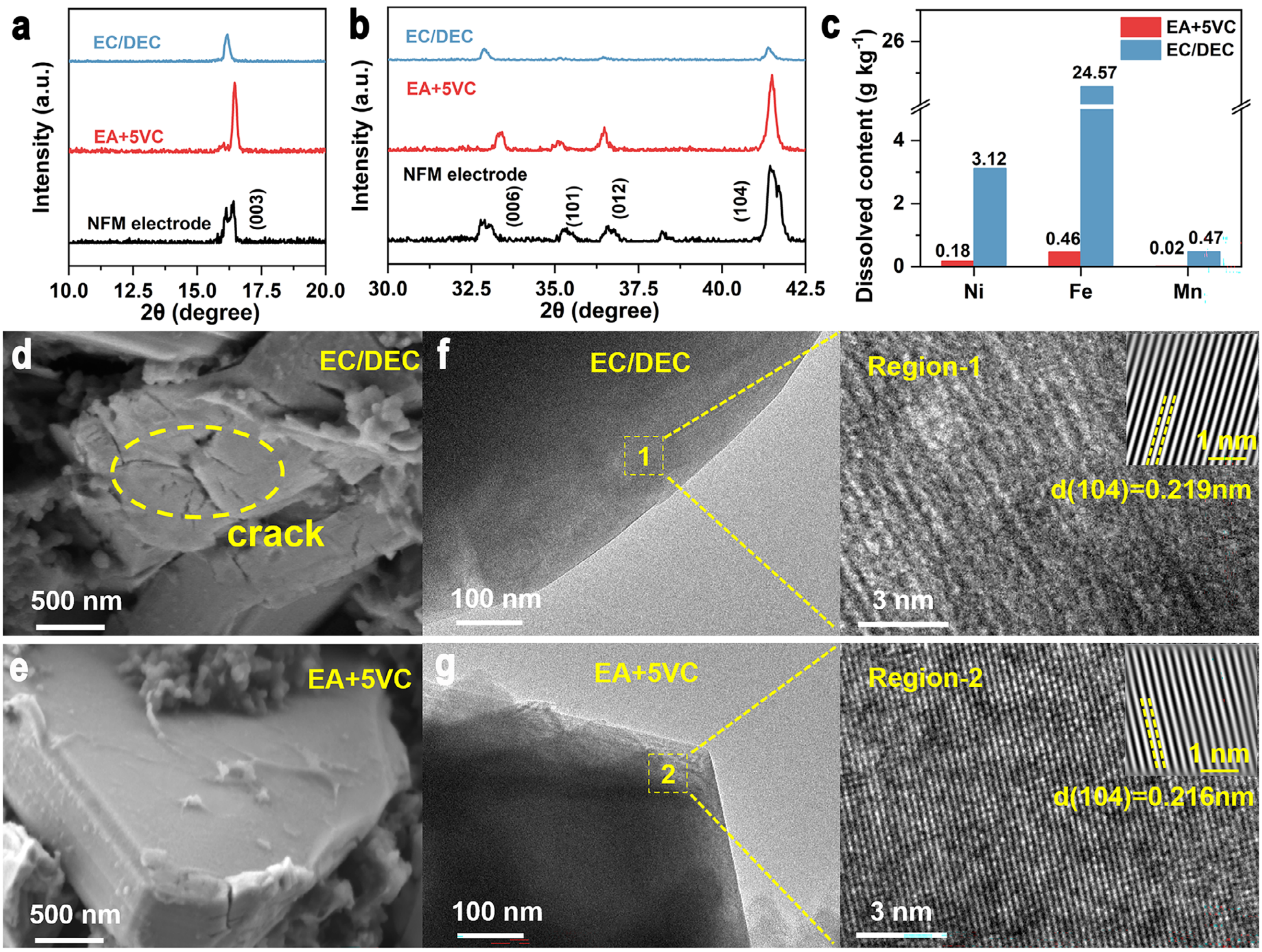

FIGURE 3 | (a,b) XRD patterns of fresh NFM electrode and the NFM electrode after 20 cycles tested in EC/DEC and EA+5VC. (c) The content of Ni, Fe, and Mn elements deposited on the cycled anodes and separator was measured by ICP. SEM images of NFM cathode cycled in (d) EC/DEC and (e) EA+5VC. TEM images of NFM cathode cycled in (f) EC/DEC and (g) EA+5VC.

interphase that effectively enables the interfacial reactions. Galvanostatic intermittent titration technique (GITT) was employed to estimate the Na^+ diffusion coefficient in NFM cathodes in different electrolyte systems (Figure S22). Within the voltage range of 2–4.3 V, the Na^+ diffusion coefficient in the NFM cathode is significantly higher when using the EA+5VC electrolyte compared to the traditional EC/DEC electrolyte. For EA+5VC electrolyte, the Na^+ diffusion coefficient ranged from 10^{-6} to 10^{-10} cm^2 s^{-1}, exceeding most recently reported values [50, 51]. Notably, it stabilized around 10^{-9} cm^2 s^{-1} at the end of the sodiation stage (deep state-of-charge). In contrast, the Na^+ diffusion coefficient in EC/DEC was considerably lower and exhibited a fast decline at the end of the sodiation stage, due to the structural degradation of the NFM cathode [52]. The superior Na^+ diffusion kinetics afforded by the EA+5VC electrolyte enhance rate capability and mitigate structural degradation (such as phase transformation and mechanical failure) by alleviating localized stress accumulation within the cathode material.

To unravel the origin of the superior high-voltage stability, the passivation mechanism of the cathode-electrolyte interphase (CEI) was elucidated. The surface of the NFM electrode cycled in EA+5VC electrolyte for 20 cycles was analyzed by TEM. As shown in Figure 4a, a thin (~7.5 nm), uniform, and compact CEI layer is clearly visible, resulting from the controlled decomposition of the electrolyte during cycling in EA+5VC electrolyte. This homogeneous and ultrathin structure promotes uniform Na^+ transport and effectively stabilizes the NFM cathode by suppressing ongoing electrolyte decomposition. As shown in Figure 4b, further characterization via high-angle annular dark-field scanning TEM (HAADF-STEM) corroborates the presence of a uniform and conformal CEI coating on the NFM particles. Additionally, energy-dispersive X-ray spectroscopy (EDS) mappings reveal the homogeneous distribution of C, O, Mn, F, P, Fe, and Ni across the cathode surface, confirming the integral role of the VC-derived interphase in facilitating interfacial stability and ion transport.

Depth-profiling X-ray photoelectron spectroscopy (XPS) was employed to characterize the composition of the CEI layer formed on NFM cathodes cycled in the EA+5VC electrolyte under different temperatures (Figure 4c–e; Figure S23a,b). The results reveal a consistently gradient organic-inorganic dual-layer structure, albeit with composition variations tuned by operating temperature. The formation of this gradient interphase is attributed to a sequential decomposition mechanism: the

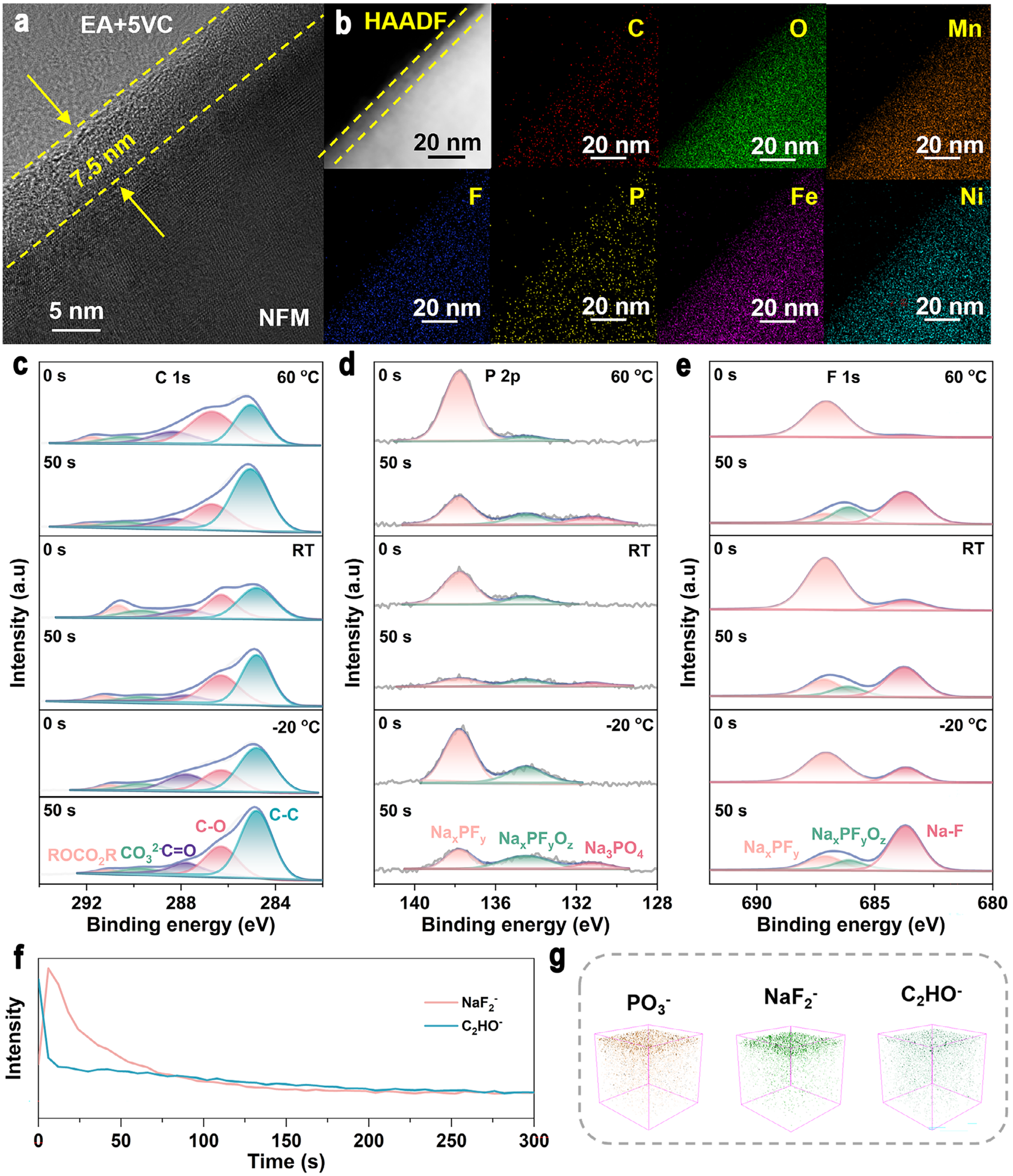

FIGURE 4 | (a) TEM images of the cycled NFM cathode after 20 cycles with EA+5VC electrolyte. (b) HAADF image of the cycled NFM cathode after 20 cycles with EA+5VC electrolyte and TEM-EDS elemental mappings of the cycled NFM cathode after 20 cycles with EA+5VC electrolyte. XPS characterization of the NFM cathode after 20 cycles with EA+5VC electrolyte under different temperatures (60°C, RT, and −20°C): (c) C 1s, (d) P 2p, (e) F 1s. (f) TOF-SIMS depth profiles of chemical fragments for CEI layer using EA+5VC and (g) corresponding 3D-mapping images of selected secondary ion fragments.

outer resilient layer consisting of poly (VC) results from the electrochemically induced ring-opening polymerization of the VC additive, while the inorganic-rich inner phase (NaF, Na_3PO_4) primarily results from the preferential decomposition of $NaPF_6$ salt. After cycling at elevated temperature (60 °C), the C 1s spectra (Figure 4c) show the distinct peaks related to the C─C (284.8 eV), C─O (286 eV), C═O (287.7 eV), and notably, $ROCO_2R$ (~291 eV) species, which can be attributed to the polymerized VC (poly(VC)) and decomposition products as the outer organic layer of CEI with high elasticity [53–55]. As the etching depth increases, the intensity of the C─O peak decreases, indicating that poly(VC) is predominantly located in the outermost surface layer. The C═O peak also exhibits higher intensity at the surface, demonstrating that the outer CEI is mainly composed of organic species and confirming the participation of VC in CEI formation. When the operating temperature decreased to −20°C), the signals of C-based species were not changed obviously at the CEI, while the portion of C─O species was lower at −20°C than those at RT and 60°C.

The P 2p spectra (Figure 4d) were analyzed to illustrate the decomposition of PF_6^- anions. Strong peaks related to the Na_xPF_y species were detected at 137.8 eV, and a very weak peak related to the $Na_xP_yFO_z$ (134.5 eV) is also observed at the surface before etching at 60 °C, attributed to the anions or their incomplete decomposition species [56]. After etching, the relatively strong $Na_xP_yFO_z$ peak and a new phosphorus-containing inorganic species of Na_3PO_4 (131.1 eV) appear, due to the increased amount of inorganic species in the inner layer. Noteworthy, when the temperature decreases, the anion-derived species increase continuously, implying that the operating temperature would slightly affect the anion-derived CEI and facilitate the inorganic-rich inner layer. Owing to its high Young's modulus and exceptional stability, Na_3PO_4 forms a dense, rigid layer within the CEI regardless of thermal conditions [57, 58]. The F 1s spectra (Figure 4e) further confirm the facilitated decomposition of anions by the change of operating temperature. The NFM electrode cycled at high temperature only demonstrates Na_xPF_y species (687.1 eV) dominated outer CEI layer, while the distinct $Na_xP_yFO_z$ and NaF species were detected after etching, ascribed to the decomposition of anions for the formation of inner CEI layer. It should also be noted that the proportion of inorganic NaF (683.7 eV) continuously increases as the temperature decreases from 60 to −20°C, indicating that PF_6^- preferentially releases F^- to generate NaF under kinetically limited conditions at lower temperature [59, 60].

Moreover, the O 1s depth profiles (Figure S23a) reveal a pronounced C─O shoulder that decays within etching, mirroring the reduced poly (VC) distribution. Concomitantly, the lattice-oxygen signal (529.8 eV) remains maximal at room temperature, confirming that the intact transition-metal-oxide framework inhibits cation dissolution [61]. Na 1s spectra (Figure S23b) further show that the NaF content increases steadily from the surface toward the interior, reinforcing the inorganic-rich subsurface. Taking all into consideration, the XPS data establish a gradient CEI architecture: a flexible, poly(VC)-dominated outer layer that accommodates mechanical strain, seamlessly transitioning to an inner ceramic matrix of Na_3PO_4 and NaF that provides high modulus and electronic insulation [62]. These results clearly demonstrated that the temperature-invariant interphase with gradient architecture enables exceptional interfacial resilience, underscoring the efficacy of VC in forming a robust interphase capable of wide-temperature operation in sodium metal batteries.

The detailed depth distribution of the CEI formed on the NFM cathode cycled in the EA+5VC electrolyte was further probed by time-of-flight secondary ion mass spectrometry (TOF-SIMS), as presented in Figure 4f,g, and Figure S24. After Cs^+ etching to eliminate surface contaminants, the intensities of PO_2^- and PO_3^- fragments decrease with increasing etching depth (Figure S24b), consistent with the P 2p XPS results, confirming that PF_6^- anion decomposition drives the formation of the inorganic-rich inner CEI. In contrast, the C_2HO^- signal (Figure 4f) is strongest in the near-surface region and decays rapidly with depth, corresponding to the poly (VC)-derived organic outer layer. The NaF_2^- intensity shows an initial rise followed by a decline, further indicating the enrichment of inorganic species in the subsurface region. As reconstructed in Figure 4g, these constructs a clear gradient architecture from the outside to the inside, an "organic flexible layer-inorganic enriched layer." endowing the electrode/electrolyte interface with excellent temperature robustness and electrochemical stability.

To further evaluate the compatibility of the EA+5VC electrolyte with sodium-metal anodes, Na||Na symmetric cells were assembled and tested (Figure S25). Cells employing EA+5VC exhibited stable, symmetric voltage profiles with consistently low overpotentials, indicating highly reversible sodium plating/stripping and stable interfacial impedance. In contrast, cells with EC/DEC electrolyte, despite initially displaying slightly lower overpotentials, showed a rapid increase in polarization upon cycling, accompanied by increasingly asymmetric voltage profiles. This behavior reflects the inability of the SEI formed in EC/DEC to effectively suppress non-uniform sodium deposition and dendritic growth. XPS depth profiling (Figure S26) further elucidated the distinct interfacial chemistries. In the SEI formed by EA+5VC, the intensities of the P 2p and F 1s signals were markedly stronger than those observed in the EC/DEC system, confirming the preferential decomposition of PF_6^- anions and the consequent formation of an inorganic-rich composite SEI containing NaF and Na_xPF_y. By contrast, the SEI derived from EC/DEC was predominantly composed of organic carbon/oxygen species, with minimal inorganic contribution. This compositional distinction directly correlates with the superior mechanical robustness and enhanced ionic conductivity of the SEI in the VC-modified system. Together, these results demonstrate that the VC additive promotes the formation of anion-derived interphases, enabling the simultaneous construction of robust, gradient protective layers on both electrodes-a key factor underlying the high-voltage stability and wide-temperature performance of the cells.

At −20°C (Figure 5a), the NFM||Na cell using the EA+5VC electrolyte delivers a remarkable reversible capacity of 117.4 mAh g^{-1} after 80 cycles, corresponding to a high retention rate of 91.3%, which demonstrates exceptional low-temperature performance. In contrast, the cell with EC/DEC electrolyte fails rapidly within 40 cycles. Although the EC/DEC system maintains relatively stable CE under these conditions, suggesting initially adequate interfacial charge transfer, the cell ultimately fails due to severely compromised ionic conductivity at low temperature,

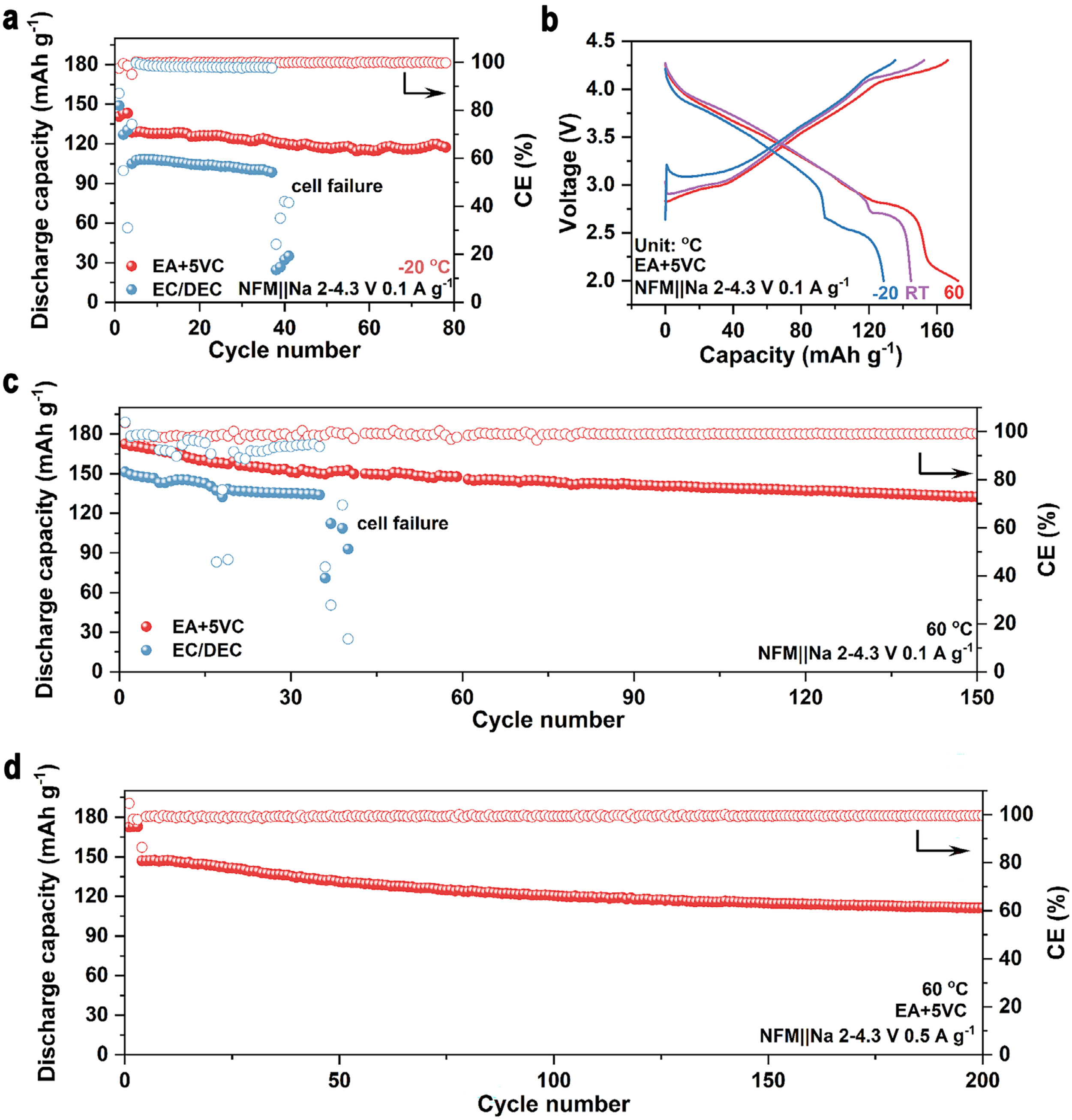

FIGURE 5 | (a) Cycling performance of NFM||Na cells using EC/DEC and EA+5VC in the voltage range of 2–4.3 V at 0.1 A g^{-1} under –20°C condition. (b) Charge-discharge curves of NFM||Na cells with EA+5VC electrolyte within 2–4.3 V at 0.1 A g^{-1} under different temperatures (60, RT, and –20°C). Cycling performance of NFM||Na cells using EC/DEC and EA+5VC in the voltage range of 2–4.3 V at 0.1 A g^{-1} under 60°C condition at (c) 0.1 A g^{-1} and (d) 0.5 A g^{-1}.

leading to irreversible damage. Moreover, even under the more extreme condition of −40°C, the cell employing the EA+5VC electrolyte remains capable of sustained cycling behavior (Figure S27), confirming that the electrolyte system retains fundamental electrochemical functionality in ultra-low-temperature environments. As illustrated in Figure 5b, the first-cycle charge-discharge profiles of the EA+5VC cell exhibit well-defined plateaus and high reversible capacities across a wide temperature range (−20°C to 60°C). Notably, the discharge capacity at 60°C exceeds that at room temperature, further underscoring the electrolyte's excellent high-temperature stability. The NFM||Na cell with EC/DEC electrolyte retains 88.8% of its room-temperature capacity at −20°C and preserves visible charge/discharge plateaus; however, it undergoes rapid failure due to ionic transport limitations. This superior wide-temperature performance is attributed to the high ionic conductivity of the EA+5VC electrolyte and the formation of a robust, temperature-resilient CEI, which together facilitate stable sodium-ion transport and interfacial kinetics across extreme operating conditions.

To assess the feasibility of EA+5VC electrolyte for wide-temperature SMBs, NFM||Na cells were evaluated under different temperatures (−20°C to 60°C). At 60°C and a current density of 0.1 A g^{-1}, the cell operates stably for 150 cycles within the voltage window from 2.0 to 4.3 V, delivering an initial discharge capacity of 170 mAh g^{-1} and an impressive capacity retention capacity of 76.8% after 150 cycles (Figure 5c), which is significantly superior to that of the EC+DEC electrolyte (failed after around 40 cycles). Even at a higher current density of 0.5 A g^{-1}, a capacity retention rate of 75.7% can still be achieved after 200 cycles (Figure 5d). The broad compatibility of this protective interphase is further demonstrated in NFPP||Na cells, which deliver a specific capacity of 94 mAh g^{-1} with 94.9% capacity retention after 200 cycles at 60°C and 0.5 A g^{-1} (2.5–4.0 V, Figure S28). These results confirm that the EA+5VC electrolyte enables the formation of a stable CEI, which effectively mitigates cathode-electrolyte side reactions and thereby enhances the high-temperature cycling stability of SMBs. Even enlarging the cathode size to a pouch cell, the NFM||Na pouch cell (Figure S29) employing the EA+5VC electrolyte and operating operated within a voltage window of 2.0–4.3 V, delivered an initial specific capacity was 107.3 mAh g^{-1}. and retained 85.7 % of its capacity over 60 cycles, demonstrating stable cycling performance and confirming the practical viability of the EA+5VC electrolyte.

3 | Conclusion

In summary, we have pioneered a vinylene carbonate (VC)-modified ethyl acetate (EA)-based electrolyte that for the first time enables high-voltage and wide-temperature operation of sodium-ion batteries down to −40°C, marking a significant advancement beyond the conventional oxidation voltage limits of carboxylate ester electrolytes. The introduction of VC not only enhances the oxidative stability of the EA electrolyte but also promotes the formation of an ultrathin yet robust gradient cathode-electrolyte interphase (CEI). This CEI exhibits a fluorine-rich organic exterior that ensures flexibility and an inorganic-rich interior (comprising NaF and Na_3PO_4) that enhances mechanical strength and ionic conduction, collectively stabilizing the O3-type NFM cathode under harsh operational conditions. As a result, the NFM||Na cell exhibits remarkable cycling stability under extreme conditions, including high voltage (4.5 V), low temperature (−20°C), and elevated temperature (60°C). Furthermore, the NFM||HC full cell demonstrates high reversibility with an average Coulombic efficiency of 99.3% over 100 cycles, underscoring the practical viability of this electrolyte system. The practicality of this electrolyte is further validated in cells with $Na_4Fe_3(PO_4)_2(P_2O_7)$ (NFPP) polyanionic cathodes, underscoring its potential for industrial application. This work introduces a new design strategy for carboxylate-based electrolytes that simultaneously achieves wide-temperature operation and high-voltage stability through rational additive engineering, providing valuable insights toward the development of advanced sodium-ion batteries for energy storage systems.

Acknowledgements

This work was financially supported by the National Natural Science Foundation of China (52307236), the China Postdoctoral Science Foundation (2023M730885), and the Postdoctoral Science Foundation of Heilongjiang Province (LBH-Z23197). J. W. thanks the Opening Funding from Key Laboratory of Engineering Dielectrics and Its Application (Ministry of Education) (No. KFM202507), the Open Project of Inner Mongolia Engineering Research Center of Lithium–Sulfur Battery Energy Storage (No. MDK2025071), and the fellowship supported by Alexander von Humboldt Foundation. H.L. also acknowledges the Young Science and Technology Talent Support Project of the Heilongjiang Association for Science and Technology (2023QNTJ009). The authors gratefully acknowledge Shanghai Rukun New Materials Co., Ltd. for providing the chemicals used for electrolyte preparation.

Open access funding enabled and organized by Projekt DEAL.

Conflicts of Interest

The authors declare no conflict of interest.

Data Availability Statement

The data that support the findings of this study are available from the corresponding author upon reasonable request.

References

1. Q. Wang, D. Zhou, C. Zhao, et al., "Fast-Charge High-Voltage Layered Cathodes for Sodium-Ion Batteries," *Nature Sustainability* 7 (2024): 338–347.

2. C. Wang, C. Zhu, D. Wu, et al., "Nonflammable Electrolyte Interfacial and Solvation Chemistry for High-Voltage Sodium Metal Batteries," *Advanced Functional Materials* 35 (2025): 2500258.

3. H. Li, F. Wu, J. Wang, et al., "Anode-Free Sodium Metal Batteries: Optimisation of Electrolytes and Interphases," *Energy & Environmental Science* 18 (2025): 3887–3916.

4. J. Huang, K. Wu, G. Xu, M. Wu, S. Dou, and C. Wu, "Recent Progress and Strategic Perspectives of Inorganic Solid Electrolytes: Fundamentals, Modifications, and Applications in Sodium Metal Batteries," *Chemical Society Reviews* 52 (2023): 4933–4995.

5. K. Xie, Y. Ji, L. Yang, and F. Pan, "Electrolyte Design Strategies to Construct Stable Cathode-Electrolyte Interphases for High-Voltage Sodium-Ion Batteries," *Advanced Energy Materials* 15 (2025): 2405301.

6. Q. Gui, B. Xu, K. Yu, et al., "Comparison of $NaNi_{1/3}Fe_{1/3}Mn_{1/3}O_2$ and $Na_4Fe_3(PO_4)_2(P2O_7)$ Cathode Sodium-Ion Battery Behavior Under Overcharging Induced Thermal Runaway," *Chemical Engineering Journal* 497 (2024): 154732.

7. S. Chen, W. Zhao, G. Zheng, et al., "Engineering Durable Interphases for High-Voltage Li-Ion Batteries Under Thermal Stress," *National Science Review* 12 (2025): nwaf345.

8. X. He, J. Deng, N. Feng, et al., "Engineering Anionic Aggregation in Dilute Electrolyte for High Performance Layered Oxide Cathodes for Sodium-Ion Batteries," *Angewandte Chemie International Edition* 65 (2026): e22923.

9. X. Zheng, Z. Cao, Z. Gu, et al., "Toward High Temperature Sodium Metal Batteries via Regulating the Electrolyte/Electrode Interfacial Chemistries," *ACS Energy Letters* 7 (2022): 2032–2042.

10. D. Peng, R. Sun, J. Han, et al., "A Low-Concentrated Electrolyte With a 3.5 V Electrochemical Stability Window, Made by Restructuring the H-Bond Network, for High-Energy and Long-Life Aqueous Sodium-Ion Batteries," *ACS Energy Letters* 9 (2024): 6215–6224.

11. D. Wu, H. Wang, C. Zhu, C. Wang, X. Li, and J. Ma, "Highly Safe Electrolyte for Fast-Charging, High-Temperature, High-Voltage Sodium Metal Batteries," *Advanced Functional Materials* 35 (2025): 2423841.

12. W. Guo, X. Liu, Y. Mu, et al., "Outside-in Directional Sodium Deposition Through Self-Supporting Gradient Fluorinated Magnesium Alloy Framework Toward High-Rate Anode-Free Na Batteries," *Energy Storage Materials* 73 (2024): 103840.

13. Y. Bai, X. Zheng, H. Liu, et al., "Honeycomb-Like Superstructure of 3D Sodiophilic Host for Anode-Free Sodium Batteries," *Energy Storage Materials* 74 (2025): 103926.

14. Q. Wang, F. Liu, Z. Qi, G. Qin, L. Wang, and X. He, “UV-Triggered In Situ Formation of a Robust SEI on Black Phosphorus for Advanced Energy Storage: Boosting Efficiency and Safety via Rapid Charge Integration Plasticity,” *Advanced Energy Materials* 15 (2024): 2403188.

15. M. Moorthy, B. Moorthy, B. K. Ganesan, et al., “A Series of Hybrid Multifunctional Interfaces as Artificial SEI Layer for Realizing Dendrite Free, and Long-Life Sodium Metal Anodes,” *Advanced Functional Materials* 33 (2023): 2300135.

16. X. Xia, S. Xu, F. Tang, et al., “A Multifunctional Interphase Layer Enabling Superior Sodium-Metal Batteries Under Ambient Temperature and −40°C,” *Advanced Materials* 35 (2023): 2209511.

17. Q. Liu, Y.-H. Feng, X. Zhu, et al., “Stabilizing Cathode-Electrolyte Interphase by Localized High-Concentration Electrolytes for High-Voltage Sodium-Ion Batteries,” *Nano Energy* 123 (2024): 109389.

18. Y. Liu, L. Zhu, E. Wang, et al., “Electrolyte Engineering With Tamed Electrode Interphases for High-Voltage Sodium-Ion Batteries,” *Advanced Materials* 36 (2024): 2310051.

19. H. Qu, Y. Wang, J. Wang, et al., “Dual-Additive-Driven Boron-Enriched Interphases Stabilize Tetrahydrofuran-Based Electrolytes for High-Voltage Sodium-Ion Batteries,” *Advanced Functional Materials* (2025): 23515, https://doi.org/10.1002/adfm.202523515.

20. K. Kim, H. Ma, S. Park, and N.-S. Choi, “Electrolyte-Additive-Driven Interfacial Engineering for High-Capacity Electrodes in Lithium-Ion Batteries: Promise and Challenges,” *ACS Energy Letters* 5 (2020): 1537–1553.

21. S. Chen, Z. Gong, P. Zhao, et al., “Design of Nanostructure in Solid Electrolyte Interphase for Enhancing the Mechanical Durability of Lithium Metal Anode by Deep-Learning Approach,” *Energy Storage Materials* 65 (2024): 103096.

22. Y. Mu, F. Chu, B. Wang, et al., “Manipulating Crystallographic Growth Orientation by Cation-Enhanced Gel-Polymer Electrolytes Toward Reversible Low-Temperature Zinc-Ion Batteries,” *InfoMat* 6 (2024): 12611.

23. S. Huang, Y. P. Huang, Y. Xia, et al., “High Li^+ Coordinated Solvation Sheaths Enable High-Quality Li Metal Anode,” *InfoMat* 5 (2023): 12411.

24. F. Wu, A. Mullaliu, T. Diemant, et al., “Beneficial Impact of Lithium Bis (Oxalato) Borate as Electrolyte Additive for High-Voltage Nickel-Rich Lithium-Battery Cathodes,” *InfoMat* 5 (2023): 12462.

25. Y. Yang, N. Yao, Y. X. Yao, et al., “Fire-Resistant Carboxylate-Based Electrolyte for Safe and Wide-Temperature Lithium-Ion Batteries,” *Advanced Energy Materials* 15 (2024): 2403183.

26. Y. Qin, S.-G. Choi, L. Mason, J. Liu, Z. Li, and T. Gao, “Carboxylate Ester-Based Electrolytes for Na-Ion Batteries,” *Chemical Science* 15 (2024): 9224–9239.

27. Z. Li, Y. X. Yao, M. Zheng, et al., “Electrolyte Design Enables Rechargeable $LiFePO_4$ /Graphite Batteries From −80 °C to 80 °C,” *Angewandte Chemie* 137 (2025): 202409409.

28. Y. Wan, X. Shi, Z. Zhou, et al., “Ion–Dipole Interactions Modulated Anion-Reinforced Solvation Chemistry for Advanced Wide-Temperature Sodium-Ion Full Batteries,” *Journal of the American Chemical Society* 147 (2025): 29939–29948.

29. Y. Gao, Z. Wang, H. Tu, et al., “Low-Temperature and Fast-Charging Sodium Metal Batteries Enabled by Molecular Structure Regulation of Fluorinated Solvents,” *Advanced Functional Materials* 35 (2024): 2414652.

30. Z. Li, N. Yao, L. Yu, et al., “Inhibiting Gas Generation to Achieve Ultralong-Lifespan Lithium-Ion Batteries at Low Temperatures,” *Matter* 6 (2023): 2274–2292.

31. M. Mao, X. Ji, Q. Wang, et al., “Anion-Enrichment Interface Enables High-Voltage Anode-Free Lithium Metal Batteries,” *Nature Communications* 14 (2023): 1082.

32. R. Jayakumar, T. P. Pollard, O. Borodin, et al., “Weakly Solvating Ester Electrolyte for High Voltage Sodium-Ion Batteries,” *Nano Energy* 128 (2024): 109969.

33. S. Zhou, X. Chen, X. Zhang, et al., “Recent Progress on Organic Liquid Electrolyte for High-Temperature Sodium Batteries,” *Advanced Functional Materials* 35 (2025): 2418784.

34. S. Lin, Z. Yang, J. Chen, Y. Qiao, L. Li, and S. Chou, “Functional Electrolyte Additives for Sodium-Ion and Sodium-Metal Batteries: Progress and Perspectives,” *Advanced Functional Materials* 34 (2024): 2400731.

35. S. Bolloju, N. Vangapally, Y. Elias, S. Luski, N.-L. Wu, and D. Aurbach, “Electrolyte Additives for Li-Ion Batteries: Classification by Elements,” *Progress in Materials Science* 147 (2025): 101349.

36. X. He, Y. Zhang, H. Li, et al., “Dual-Descriptor Tailoring: Rational Solvent Molecule Tuning Enables High-Voltage Li-Ion Batteries,” *Advanced Materials* 37 (2025): 2417076.

37. W. Kuang, X. Zhou, Z. Fan, et al., “Sulfur-Containing Inorganic-Rich Interfacial Chemistry Empowers Advanced Sodium-Ion Full Batteries,” *ACS Energy Letters* 9 (2024): 4111–4118.

38. M. D. Bhatt and C. O’Dwyer, “The Role of Carbonate and Sulfite Additives in Propylene Carbonate-Based Electrolytes on the Formation of SEI Layers at Graphitic Li-Ion Battery Anodes,” *Journal of The Electrochemical Society* 161 (2014): A1415.

39. Y. Li, B. Wen, N. Li, et al., “Electrolyte Engineering to Construct Robust Interphase With High Ionic Conductivity for Wide Temperature Range Lithium Metal Batteries,” *Angewandte Chemie International Edition* 64 (2024): 202414636.

40. L. Che, Z. Hu, T. Zhang, et al., “Regulating the Interfacial Chemistry of Graphite in Ethyl Acetate-Based Electrolyte for Low-Temperature Li-Ion Batteries,” *Battery Energy* 3 (2024): 20230064.

41. C. D. Qiu, Y. Hu, K. Cao, et al., “Engineering Peculiar Cathode Electrolyte Interphase Toward Sustainable and High-Rate Li–S Batteries,” *Advanced Energy Materials* 13 (2023): 2300229.

42. S. Wu, J. Zhou, Q. Li, and F. Wu, “Natural Gluten Binder Enabling High-Performance Hard Carbon Anode in Sodium-Ion Batteries,” *Advanced Functional Materials* 35 (2025): 2507916.

43. X. Jiang, H. Zhang, Y. Qu, et al., “Engineering Electrolyte Strong-Weak Coupling Effect Toward Wide-Temperature Supercapacitor,” *Energy Storage Materials* 68 (2024): 103374.

44. M. Ma, B. Chen, Y. Tu, and H. Pan, “Ternary Electrolyte Enables High-Voltage and High-Temperature Na-Ion Batteries,” *ACS Energy Letters* 9 (2024): 4655–4665.

45. Z. Wang, T. Zheng, S. Wang, et al., “Topological Design of Highly Conductive Weakly Solvating Electrolytes for Ultrastable Sodium Metal Batteries Operating at −60°C and Below,” *Journal of the American Chemical Society* 147 (2025): 5962–5970.

46. Z. Huang, Z. Xiao, H. Zhang, et al., “Temperature-Robust Solvation Enabled by Solvent Interactions for Low-Temperature Sodium Metal Batteries,” *Journal of the American Chemical Society* 147 (2025): 5162–5171.

47. X. He, J. Peng, Q. Lin, et al., “Sulfolane-Based Flame-Retardant Electrolyte for High-Voltage Sodium-Ion Batteries,” *Nano-Micro Letters* 17 (2024): 45.

48. Y. Liu, Y. Ying, L. Fei, et al., “Valence Engineering via Selective Atomic Substitution on Tetrahedral Sites in Spinel Oxide for Highly Enhanced Oxygen Evolution Catalysis,” *Journal of the American Chemical Society* 141 (2019): 8136–8145.

49. X. Luo, L. Wang, M. Tian, et al., “Cu/Mg Substitution Enables O3-Type $NaNi_{0.4}Fe_{0.2}Mn_{0.4}O_2$ Cathode Material with Simpler Phase Transition Process for Sodium-Ion Batteries,” *Journal of Alloys and Compounds* 1014 (2025): 178713.

50. Y. H. Feng, M. Liu, J. Wu, et al., “Monolithic Interphase Enables Fast Kinetics for High-Performance Sodium-Ion Batteries at Subzero Temperature,” *Angewandte Chemie International Edition* 63 (2024): 202403585.

51. L. Li, R. Li, X. Cao, J. Bai, W. Dong, and C. Zhang, “Enhanced Sodium Storage Performance of Floral Spherical Vanadium Disulfide by

Ether-Based Electrolyte and Copper Collector Inducing," *Small* 21 (2025): 2501371.

52. Q. Wang, G. Yu, B. Luo, et al., "Suppression of Adverse Phase Transition of Layered Oxide Cathode via Local Electronic Structure Regulation for High-Capacity Sodium-Ion Batteries," *ACS Nano* 18 (2024): 18622.

53. J. Li, S. Sui, X. Zhou, et al., "Weakly Coordinating Diluent Modulated Solvation Chemistry for High-Performance Sodium Metal Batteries," *Angewandte Chemie International Edition* 63 (2024): 202400406.

54. S. Park, S. Y. Jeong, T. K. Lee, et al., "Replacing Conventional Battery Electrolyte Additives with Dioxolone Derivatives for High-Energy-Density Lithium-Ion Batteries," *Nature Communications* 12 (2021): 838.

55. T. Jaumann, J. Balach, U. Langklotz, et al., "Lifetime vs. Rate Capability: Understanding the Role of FEC and VC in High-Energy Li-Ion Batteries with Nano-Silicon Anodes," *Energy Storage Materials* 6 (2017): 26–35.

56. P. M. L. Le, T. D. Vo, K. M. Le, et al., "Synergetic Dual-Additive Electrolyte Enables Highly Stable Performance in Sodium Metal Batteries," *Small* 20 (2024): 2402256.

57. Y. Huang, Q. Zhang, X. G. Sun, et al., "Multiple Functional Bonds Integrated Interphases for Long Cycle Sodium-Ion Batteries," *Angewandte Chemie International Edition* 63 (2024): 202406277.

58. Y. H. Feng, M. Liu, W. Qi, et al., "Dual-Anionic Coordination Manipulation Induces Phosphorus and Boron-Rich Gradient Interphase Towards Stable and Safe Sodium Metal Batteries," *Angewandte Chemie International Edition* 64 (2024): 202415644.

59. Q. Yu, Y. Xiao, S. Zhao, et al., "All-Fluorinated Low-Solvation Electrolytes for High-Voltage Sodium Metal Batteries With Appealing Stability," *Advanced Functional Materials* 34 (2024): 2401868.

60. J. Zhang, N. Sawut, H. Fan, et al., "Alleviating Self-Discharge in Sodium-Ion Batteries Via Functional Dual-Salt Electrolytes," *Nano Energy* 136 (2025): 110744.

61. C. Hu, L. Dai, F. Huang, et al., "Carboxylate-Based Electrolyte with Bilateral Functions Enable Working Sodium-Metal Batteries at −60°C," *Angewandte Chemie International Edition* 64 (2025): 202508584.

62. Y. Zhan, P. Zhai, T. Song, W. Yang, and Y. Li, "Enhanced Performance in Lithium Metal Batteries: A Dual-Layer Solid Electrolyte Interphase Strategy Via Perfluoropolyether Derivative Additive," *Chemical Engineering Journal* 491 (2024): 151974.

Supporting Information

Additional supporting information can be found online in the Supporting Information section.

Supporting File: adfm74509-sup-0001-SuppMat.docx.